

Peridynamic State-Based Models and the Embedded-Atom Model

Pablo Seleson^{1*}, Michael L. Parks² and Max Gunzburger³

¹ *Institute for Computational Engineering and Sciences, 201 East 24th St, Stop C0200, Austin, Texas 78712-1229, USA.*

² *Sandia National Laboratories, Computing Research Center, P.O. Box 5800, MS 1320, Albuquerque, NM 87185-1320, USA.*

³ *Department of Scientific Computing, 400 Dirac Science Library, Florida State University, Tallahassee, FL 32306-4120, USA.*

Received 8 December 2011; Accepted (in revised version) 30 April 2013

Communicated by Qiang Du

Available online 15 August 2013

Abstract. We investigate connections between nonlocal continuum models and molecular dynamics. A continuous upscaling of molecular dynamics models of the form of the embedded-atom model is presented, providing means for simulating molecular dynamics systems at greatly reduced cost. Results are presented for structured and structureless material models, supported by computational experiments. The nonlocal continuum models are shown to be instances of the state-based peridynamics theory. Connections relating multibody peridynamic models and upscaled nonlocal continuum models are derived.

AMS subject classifications: 45K05, 70F10, 74H15

PACS: 46.15.-x, 02.30.Rz, 46.40.Cd, 34.20.Cf

Key words: Peridynamics, multibody potentials, embedded-atom, molecular dynamics.

1 Introduction

Multibody potentials were proposed in molecular dynamics (MD) to overcome some of the limitations of pair potentials [1, Section 4.3]. One such multibody potential is the *embedded-atom model* (EAM) [2, 3], commonly used for metallic systems, in which the potential energy of the system is expressed as a combination of volume-dependent and

*Corresponding author. *Email addresses:* seleson@ices.utexas.edu (P. Seleson), mlparks@sandia.gov (M. L. Parks), gunzburg@fsu.edu (M. Gunzburger)

pair potential energy terms. Other common many-body potentials include the Stillinger-Weber potential [4], frequently used for modeling semiconductors, and the Tersoff potential [5], which utilizes two- and three-atom contributions and is based on the idea that the strength of a bond between two atoms is environment dependent.

MD models are computationally expensive and even intractable at large scales. In contrast, continuum models can be discretized on coarse meshes, resulting in efficient numerical implementations. Consequently, attempts to replace MD models by continuum models, capable of preserving important features of MD, have been proposed. One such approach, based on higher-order gradient continuum models, is given in [6]. A different approach, using nonlocal continuum models (NCMs) appears in [7]. These methods attempt to use continuum models for the *continuous upscaling*[†] of MD. By replacing MD models with their corresponding upscaled continuum models, we can simulate length scales not tractable by MD alone. In [7], the continuous upscaling of pairwise MD models is derived within the peridynamics theory of solid mechanics [8,9], recovering characteristic dispersion relations of discrete models at the continuum level. That work is related to coarse-graining, but differs from the phase-space average approach presented in [10]. In this paper, we extend the techniques of [7] to many-body potentials of the form of the MD EAM. We derive upscaled nonlocal continuum models inspired by peridynamics, and we demonstrate that all of the nonlocal continuum models we derive are instances of the peridynamics theory.

Alternative approaches for efficient and accurate simulation of systems exhibiting MD phenomena include concurrent multiscale modeling. These methods appear in the literature under so-called atomistic-to-continuum coupling methods, attempting to couple classical continuum models and MD models [11–13].

The organization of this paper is as follows. In Section 2, we review the many-body MD EAM. The continuous upscaling of MD models to NCMs is shown for a structureless EAM in Section 3 and for a structured EAM in Section 4, with supporting computational examples. Concluding remarks are presented in Section 5. Appendix A includes an overview of the peridynamics theory and its many-body models, their connections, and their relations to upscaled NCMs.

2 Embedded-atom models in molecular dynamics

The MD EAM was proposed in [2,3] based on density functional theory and, in particular, on the earlier quasiatom [14] and effective medium [15] theories. By utilizing a volume-dependent energy, this model overcomes existing difficulties of pair potentials in the description of elastic properties of materials.

In a solid, each atom can be viewed as an impurity embedded in a host composed by all other atoms. As the energy of an impurity is a functional of the electron density of the

[†]By *continuous upscaling*, we refer to the process of deriving a continuum model from a discrete one, so that the continuum model preserves certain quantities of interest of the discrete model.

unperturbed host, the cohesive energy of the solid can be calculated from the embedding energy. In the MD EAM, then, each atom is viewed as embedded in a host lattice consisting of all other atoms, and an electron density is thus used for calculations. The potential energy of the system, denoted by E_{pot} , is taken as the sum of individual contributions

$$E_{\text{pot}} = \sum_i F_i(\rho_{h,i}) + \frac{1}{2} \sum_{\substack{i,j \\ i \neq j}} \phi_{ij}(r_{ij}), \quad (2.1)$$

where $\phi_{ij}(r_{ij})$ is a core-core repulsive pair potential between atoms i and j separated by the distance r_{ij} (a short-range electrostatic potential), and $F_i(\rho_{h,i})$ is the energy to embed atom i in the host electron density $\rho_{h,i}$. The host electron density $\rho_{h,i}$ at atom i is a linear superposition of the electron densities of constituent atoms [16], written as

$$\rho_{h,i} = \sum_{j(\neq i)} f_j(r_{ij}), \quad (2.2)$$

with f_j the electron density contributed by atom j as a function of the distance from its center. The equation of motion of atom i in a system described by the MD EAM is

$$m_i \frac{d^2 \mathbf{y}_i}{dt^2} = - \sum_{j(\neq i)} \left[F'_i(\rho_{h,i}) f'_j(r_{ij}) + F'_j(\rho_{h,j}) f'_i(r_{ij}) + \phi'_{ij}(r_{ij}) \right] \frac{\mathbf{y}_i - \mathbf{y}_j}{r_{ij}} + \mathbf{f}_i^{\text{ext}}, \quad (2.3)$$

where m_i is the mass of atom i , $\mathbf{y}_i = \mathbf{y}_i(t)$ is the position of atom i at time t , $r_{ij} := \|\mathbf{y}_i - \mathbf{y}_j\|$, and $\mathbf{f}_i^{\text{ext}} = \mathbf{f}_i^{\text{ext}}(t)$ is the external force acting on atom i at time t . We denote by F'_i the derivative of F_i with respect to its argument $\rho_{h,i}$, and similarly for f'_i and ϕ'_{ij} . In (2.3), we have omitted the time dependence for brevity. Furthermore, it is assumed that $\phi_{ij} = \phi_{ji}$.

Analytical expressions for F_i and ϕ_{ij} in (2.1) are not provided in the first MD EAMs proposed [2,3]. These functions were determined empirically from the physical properties of the solid, with the pair potential assigned a Coulombic form as $\phi_{ij}(r) = Z_i(r)Z_j(r)/r$, with $Z_i(r)$ an effective charge for the atom i . A consistent set of embedding functions and short-range repulsive pair interactions for the fcc metals Cu, Ag, Au, Ni, Pd, and Pt as well as the alloy combination of these elements is provided in [17]. These functions were determined empirically by fitting the predicted results to the sublimation energy, equilibrium lattice constant, elastic constants, and vacancy-formation energy of the pure metals as well as to the heats of solution of binary alloys.

In [18], a simple analytical fcc model was developed, matching the energy functional of the MD EAM with an expression for the energy previously derived in [19]. Unfortunately, the authors considered only nearest-neighbor interactions, giving only the first-order effects of the model. That model was extended beyond nearest neighbors in [20] for fcc and hcp metals, but only for electron densities which deviate less than 10% from equilibrium. Analytical expressions for the MD EAM, valid for any choice of cutoff distance, were introduced in [21]. The authors followed a similar approach as in [18], deriving $F(\rho)$ using the energy expression of [19] while taking a different functional form for the electron density functions in order to allow for multiple-neighbor interactions.

3 Continuous upscaling of a structureless embedded-atom model

The high computational cost of MD simulations motivates the development of continuum models capable of preserving dynamics and length scales of MD. These continuum models can be discretized on coarse meshes, producing substantial computational savings.

In most MD models the interaction between atoms depends only upon the current configuration; see, e.g., the dependence upon r_{ij} in (2.1) and (2.2). We refer to these types of material models as *structureless*. In Section 3.1, we demonstrate how to upscale a structureless MD EAM to a NCM, following similar derivations for the continuous upscaling of a Lennard-Jones MD model presented in [7]. In Section 3.2, we present numerical results for one-dimensional wave propagation showing a speedup of $15\times$ over MD.

We refer the reader to Section A.3.1, where we demonstrate that our NCM (3.4) is an instance of a generalized EAM-like peridynamic model.

3.1 An upscaled structureless embedded-atom model

Let's assume for simplicity a homogeneous system, i.e., a monatomic crystal. The MD EAM potential energy per atom for such system is (*cf.* (2.1) and (2.2))

$$E_i = F(\rho_{h,i}) + \frac{1}{2} \sum_{j(\neq i)} \phi(r_{ij}) \quad \text{with} \quad \rho_{h,i} = \sum_{j(\neq i)} f(r_{ij}). \quad (3.1)$$

In structureless materials, such as (3.1), it is customary to introduce for efficiency a cutoff radius. Two atoms are then assumed to interact directly whenever their distance is smaller than the cutoff radius. For that purpose, we define the cutoff function

$$g(x) \begin{cases} = 1, & x \leq 0, \\ \in (0,1), & 0 < x < 1, \\ = 0, & x \geq 1, \end{cases} \quad (3.2)$$

where $x := (r - r_n) / (r_c - r_n)$ with r the distance between two atoms, and the cutoff parameters r_c and r_n are given. The function $g(x)$ is assumed monotonic and continuously differentiable.

We now express (3.1) with dimensionless functions (marked with a tilde) and the cutoff function as follows:

$$E_i = E_c \tilde{F}\left(\frac{\rho_{h,i}}{\rho_e}\right) + \frac{1}{2} \sum_{j(\neq i)} \phi_e \tilde{\phi}\left(\frac{r_{ij}}{\mu}\right) g\left(\frac{r_{ij} - r_n}{r_c - r_n}\right) \quad \text{with} \quad \rho_{h,i} = f_e \sum_{j(\neq i)} \tilde{f}\left(\frac{r_{ij}}{\mu}\right) g\left(\frac{r_{ij} - r_n}{r_c - r_n}\right),$$

where E_c and ϕ_e are energy scales, μ is a length scale, and f_e and ρ_e are electronic density constants. For a perfect crystal the atoms can be distributed in shells, allowing us to write

the potential energy density per atom as

$$e := \frac{E_c}{v_a} \tilde{F}\left(\frac{\rho_h}{\rho_e}\right) + \frac{1}{2} \sum_m s_m \frac{\phi_e}{v_a} \tilde{\phi}\left(\frac{r_m}{\mu}\right) g\left(\frac{r_m - r_n}{r_c - r_n}\right) \quad \text{with} \quad \rho_h = f_e \sum_m s_m \tilde{f}\left(\frac{r_m}{\mu}\right) g\left(\frac{r_m - r_n}{r_c - r_n}\right), \quad (3.3)$$

v_a the Wigner-Seitz cell of the crystal, r_m the distance of the m -th-neighbor shell with respect to a given atom, and s_m the number of atoms in that shell. For a perfect crystal $r_m = p_m r_1$, where the constants p_m depend on the type of crystal structure. For instance, $p_m = \sqrt{m}$ in fcc crystals.

Our goal is to derive an upscaled NCM consistent with the MD EAM (3.1). Matching models is usually done with respect to certain quantities of interest (QoIs). In our case, we choose the potential energy density per particle (3.3) as our QoI and derive a continuum model that preserves this QoI under isotropic deformations. Matching energies is a standard practice in the atomistic-to-continuum coupling literature (see, e.g., [11, p. R39] and [22]).

Let $r_n = n r_{1e}$, $r_c = c r_{1e}$, and $\mu = \sigma r_{1e}$ with n , c , and σ constant. The m -th-nearest-neighbor distance in equilibrium is r_{me} , $m = 1, 2, \dots$. Assume an isotropic deformation, i.e., $r_m = \chi r_{me} = \chi p_m r_{1e}$ with χ a constant. Then,

$$e = e_c \tilde{F}\left(\frac{\rho_h}{\rho_e}\right) + \frac{1}{2} \sum_m s_m \varphi_e \tilde{\phi}\left(\frac{\chi p_m}{\sigma}\right) g\left(\frac{\chi p_m - n}{c - n}\right) \quad \text{with} \quad \frac{\rho_h}{\rho_e} = \frac{f_e}{\rho_e} \sum_m s_m \tilde{f}\left(\frac{\chi p_m}{\sigma}\right) g\left(\frac{\chi p_m - n}{c - n}\right),$$

where $e_c := E_c / v_a$ and $\varphi_e := \phi_e / v_a$. The QoI remains constant for different ‘‘resolutions’’ (i.e., different values of r_{1e}) provided that we keep constant the energy density scales e_c and φ_e , the number of interacting shells, the parameters c , n , and σ , the ratio f_e / ρ_e , the number of atoms per shell s_m , and the inter-shell parameters p_m .

Remark 3.1. We have derived a set of coarse-grained models of the form of (2.3) that preserve the potential energy density per particle of a reference MD model under isotropic deformations. The characteristic length scale of a particular coarse-grained system is determined by r_{1e} .

To proceed with the continuous upscaling of (3.1), we divide the equation of motion (2.3) by the Wigner-Seitz cell and get

$$\rho_i \frac{d^2 \mathbf{y}_i}{dt^2} = - \sum_{j(\neq i)} \left\{ \left(\bar{F}'(\rho_{h,i}) + \bar{F}'(\rho_{h,j}) \right) f'(r_{ij}) + \bar{\phi}'(r_{ij}) \right\} \frac{\mathbf{y}_i - \mathbf{y}_j}{r_{ij}} + \mathbf{b}_i,$$

where

$$\rho_i := \frac{m_i}{v_a}, \quad \bar{F}(\rho) := \frac{1}{v_a} F(\rho), \quad \bar{\phi}(r) := \frac{1}{v_a} \phi(r), \quad \text{and} \quad \mathbf{b}_i := \frac{1}{v_a} \mathbf{f}_i^{\text{ext}}.$$

Assuming continuous expressions for the fields of mass density $\rho(\mathbf{x})$, host electron density $\rho_h(\mathbf{x}, t)$, current position $\mathbf{y}(\mathbf{x}, t)$, and body force density $\mathbf{b}(\mathbf{x}, t)$, we can express the

equation of motion and host electron density, respectively, for a point \mathbf{x} in a crystal as

$$\rho(\mathbf{x}) \frac{\partial^2 \mathbf{y}}{\partial t^2}(\mathbf{x}, t) = - \sum_{\substack{n_1, n_2, n_3 \\ \mathbf{n} \neq 0}} \left[\left(\bar{F}'(\rho_h(\mathbf{x}, t)) + \bar{F}'(\rho_h(\mathbf{x} + n_i \mathbf{a}_i, t)) \right) f'(\|\mathbf{y}(\mathbf{x} + n_i \mathbf{a}_i, t) - \mathbf{y}(\mathbf{x}, t)\|) \right. \\ \left. + \bar{\phi}'(\|\mathbf{y}(\mathbf{x} + n_i \mathbf{a}_i, t) - \mathbf{y}(\mathbf{x}, t)\|) \right] \frac{\mathbf{y}(\mathbf{x}, t) - \mathbf{y}(\mathbf{x} + n_i \mathbf{a}_i, t)}{\|\mathbf{y}(\mathbf{x}, t) - \mathbf{y}(\mathbf{x} + n_i \mathbf{a}_i, t)\|} + \mathbf{b}(\mathbf{x}, t),$$

$$\rho_h(\mathbf{x}, t) = \sum_{\substack{n_1, n_2, n_3 \\ \mathbf{n} \neq 0}} f(\|\mathbf{y}(\mathbf{x} + n_i \mathbf{a}_i, t) - \mathbf{y}(\mathbf{x}, t)\|),$$

where $\{\mathbf{a}_i\}_{i=1,2,3}$ are the lattice primitive vectors, the summations over n_1, n_2, n_3 are over all integers, and the Einstein summation convention for repeated indexes is used. We now let $\mathbf{a}_i = (r_{1e}/r_{1e}^0) \mathbf{a}_i^0$, where the superscript 0 denotes a reference MD lattice. Using the three-dimensional Dirac delta function, we obtain the upscaled EAM

$$\rho \frac{\partial^2 \mathbf{y}}{\partial t^2} = \int_{\mathbb{R}^3} \left\{ \sum_{\substack{n_1, n_2, n_3 \\ \mathbf{n} \neq 0}} \left[\left(\bar{F}'(\rho_h) + \bar{F}'(\hat{\rho}_h) \right) f'(\|\hat{\mathbf{y}} - \mathbf{y}\|) + \bar{\phi}'(\|\hat{\mathbf{y}} - \mathbf{y}\|) \right] \delta^{(3)} \left(\hat{\mathbf{x}} - \left(\mathbf{x} + \frac{n_i}{\sigma} \frac{\mathbf{a}_i^0}{r_{1e}^0} \mu \right) \right) \right\} \\ \times \frac{\hat{\mathbf{y}} - \mathbf{y}}{\|\hat{\mathbf{y}} - \mathbf{y}\|} dV_{\hat{\mathbf{x}}} + \mathbf{b}, \quad (3.4)$$

$$\rho_h = \int_{\mathbb{R}^3} \sum_{\substack{n_1, n_2, n_3 \\ \mathbf{n} \neq 0}} f(\|\check{\mathbf{y}} - \mathbf{y}\|) \delta^{(3)} \left(\check{\mathbf{x}} - \left(\mathbf{x} + \frac{n_i}{\sigma} \frac{\mathbf{a}_i^0}{r_{1e}^0} \mu \right) \right) dV_{\check{\mathbf{x}}} \quad (3.5)$$

with $\rho = \rho(\mathbf{x})$, $\mathbf{y} := \mathbf{y}(\mathbf{x}, t)$, $\hat{\mathbf{y}} := \mathbf{y}(\hat{\mathbf{x}}, t)$, $\check{\mathbf{y}} := \mathbf{y}(\check{\mathbf{x}}, t)$, $\rho_h := \rho_h(\mathbf{x}, t)$, $\hat{\rho}_h := \rho_h(\hat{\mathbf{x}}, t)$, and $\mathbf{b} = \mathbf{b}(\mathbf{x}, t)$.

3.2 Numerical results

We demonstrate the continuous upscaling through a one-dimensional example. Following [21], we assume the MD EAM functions

$$F(\rho) = -E_c \left[1 - \frac{\alpha}{\beta} \ln \left(\frac{\rho}{\rho_e} \right) \right] \left(\frac{\rho}{\rho_e} \right)^{\frac{\alpha}{\beta}} + \frac{1}{2} \phi_e \sum_m s_m \left[1 + (p_m - 1) \lambda - p_m \frac{\lambda}{\beta} \ln \left(\frac{\rho}{\rho_e} \right) \right] \\ \times \exp[-(p_m - 1) \gamma] \left(\frac{\rho}{\rho_e} \right)^{p_m \frac{\gamma}{\beta}} g \left(\frac{p_m \left(1 - \frac{1}{\beta} \ln \left(\frac{\rho}{\rho_e} \right) \right) - n}{c - n} \right), \quad (3.6)$$

$$\phi(r) = -\phi_e \left[1 + \lambda \left(\frac{r}{\mu} - 1 \right) \right] \exp \left[-\gamma \left(\frac{r}{\mu} - 1 \right) \right] g \left(\frac{r - r_n}{r_c - r_n} \right), \quad (3.7)$$

$$f(r) = f_e \sum_{\ell=0}^k c_\ell \left(\frac{\mu}{r} \right)^\ell g \left(\frac{r - r_n}{r_c - r_n} \right), \quad (3.8)$$

$$g(x) = \begin{cases} 1, & x \leq 0, \\ (1-x)^3(1+3x+6x^2), & 0 < x < 1, \\ 0, & x \geq 1, \end{cases} \quad (3.9)$$

where $\alpha = (9K_e\Omega_e^a/E_c)^{1/2}$ with K the bulk modulus, Ω^a the atomic volume, and E_c the cohesive energy. The subscript e indicates evaluation at equilibrium. Adjustable parameters for $F(\rho)$ and $\phi(r)$ are $\rho_e, \beta, \phi_e, \lambda$ and γ . The parameter ρ_e can be eliminated because only ratios ρ/ρ_e appear in $F(\rho)$. For details on the fitting procedure and fitted values, including the parameters f_e and $\{c_\ell\}_{\ell=0,\dots,k}$ of the electron density function $f(r)$, see [21].

Remark 3.2. In contrast to [21, Eqs. (13) and (16)], we have explicitly included the cutoff function $g(x)$, for $\phi(r)$ and $f(r)$, in (3.7) and (3.8), respectively. As a consequence, we modify accordingly the analytical expression of $F(\rho)$ in (3.6). This is done following the same derivations leading to Equation (17) in [21].

We present one-dimensional wave propagation results for the upscaled EAM (3.4) with the functions (3.6)-(3.9). Following similar examples in [6], we choose a domain $\mathcal{B} = [0, 1000]$. The initial configuration is defined as $y(x, 0) = x + p(x)$ for all $x \in \mathcal{B}$, where $p(x)$ is a smooth 21-st order piecewise polynomial such that $p \equiv 0$ on $[0, 300] \cup [700, 1000]$, $p(500) = 7$, and $p'(x) = p''(x) = \dots = p^{(10)}(x) = 0$ for $x = 300, 500, 700$. The initial displacement, i.e., $u(x, 0) = p(x)$, is illustrated in Fig. 2(a). Similar simulations for the continuous upscaling of nonlocal linear springs and Lennard-Jones MD models were presented in [7]. The reference atomistic system is chosen to have 1,001 atoms interacting through the MD EAM (2.3) with the functions (3.6)-(3.9). We assume no external forces, i.e., $\mathbf{f}_i^{\text{ext}} = \mathbf{0}$ and $\mathbf{b} = \mathbf{0}$ in (2.3) and (3.4), respectively. We run a ‘‘fine-grid’’ NCM simulation with $N_x = 1001$ particles to compare to MD, as well as ‘‘coarse-grid’’ NCM simulations with $N_x = 501$ and $N_x = 251$.

In the simulations, we use the choices of parameters described in Table 1 with a the lattice constant in the MD system. The final simulation time is denoted by T and the time step by Δt . In the NCM simulations, we denote the mesh size by h and take, accordingly, $r_n = 3.5h$, $r_c = 3.9h$, and $\Delta t = 0.2h$. We choose $\sigma = 2$, so that $\mu = 2h$.

Table 1: Parameters for the structureless EAM defined by (3.6)-(3.9); data for Cu [18, 21].

c_0	c_1	c_2	c_3	c_4	c_5
0.14095	-1.93222	9.60043	-21.23718	20.18581	-5.81656
α	β	γ	λ	r_n	r_c
5.082	5.85	6.82054	12.06	$3.5a$	$3.9a$
ρ	E_c	ϕ_e	Δt	T	f_e/ρ_e
63.546	3.54	0.1217	$0.2a$	120	1/12.0

The numerical experiments are shown in Fig. 1. We compare the results of an MD simulation for 1,001 atoms (a,b) with a NCM simulation with the same resolution (c) and coarsened NCM simulations with 501 particles (d) and 251 particles (e). Fig. 1(a)

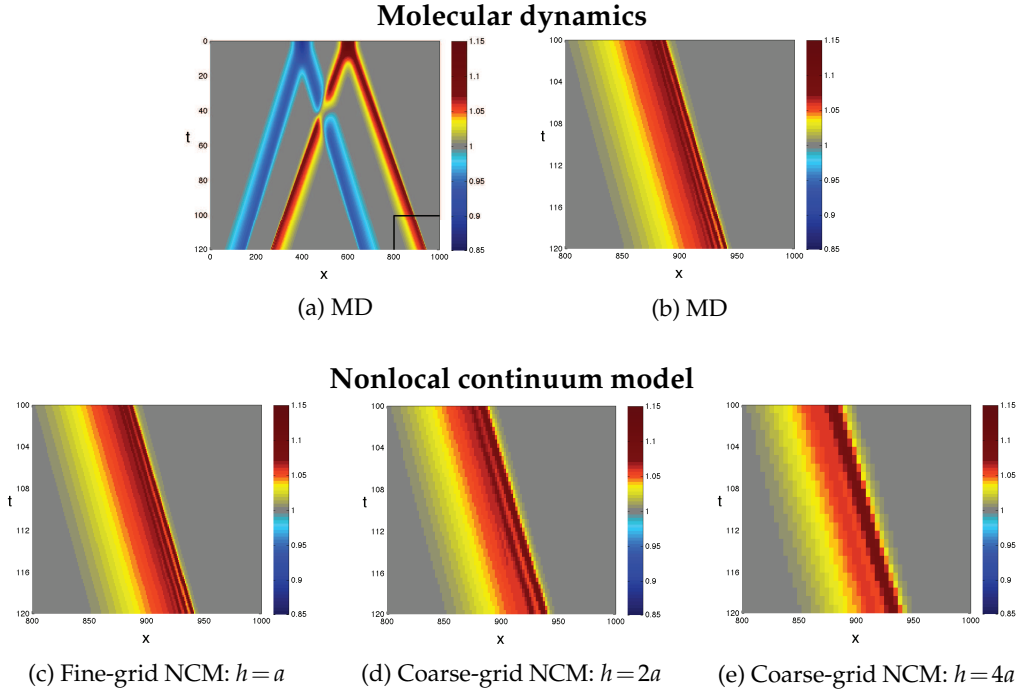


Figure 1: Mass density evolution for one-dimensional wave propagation. We compare (a,b) the molecular dynamics (MD) embedded-atom model (2.3) and (c,d,e) the upscaled nonlocal continuum model (NCM) (3.4). The MD model and NCM use the functions (3.6)-(3.9). Time is represented in the vertical axis (increasing from top to bottom) and the horizontal axis represents the atom/particle position in the reference configuration. The lattice constant in the MD simulation is denoted by a , and the mesh size in the NCM simulations is denoted by h . Each point in the plot corresponds to a given atom/particle at a specific time level. The color assigned to a point is an approximation of $(dy/dx)^{-1}$, which is proportional to the mass density. In (a), we observe the MD simulation in the complete space-time domain. Plots (b) and (c,d,e) are a zoom-in of the bottom-right corner of the entire space-time domain plots, like (a), and show the dispersion patterns produced. We omit the entire space-time domain NCM plots because they are qualitatively similar to the MD plot.

shows the MD simulation in the complete space-time domain. The remaining plots show a zoom-in of the bottom-right corner of the entire space-time domain plots, like Fig. 1(a), to better illustrate the solution. We omit the entire space-time domain NCM plots because they are qualitatively similar to the MD plot. The x -axis represents the reference position of the atoms/particles and the y -axis represents time (increasing from top to bottom). The color assigned to a point represents the quantity $(dy/dx)^{-1}$, approximated as $(x_{j+1} - x_{j-1}) / (y_{j+1} - y_{j-1})$ for atom/particle j , which is proportional to the mass density, allowing us to track the wave as it moves (*cf.* [6]). We conclude that the NCM recovers the same results as the MD model for the same resolution. For the coarse simulations, the general behavior of the MD solution is qualitatively preserved, although the oscillations that characterize the mass density of the system depend upon the resolution provided by the chosen discretization. Similar conclusions for the continuous upscaling of a Lennard-Jones MD model appear in [7].

Table 2: Comparison between the computational cost of the molecular dynamics (MD) and nonlocal continuum model (NCM) simulations. The lattice constant in the MD simulation is denoted by a , and the mesh size in the NCM simulations is denoted by h . The coarse-grid NCM simulations reduce the number of particles and time steps.

	MD	NCM ($h=2a$)	NCM ($h=4a$)
Number of atoms/particles	1001	501	251
Number of time steps	600	300	150
Total time (seconds)	153.33	38.78	9.89
Speedup	1.00	3.95	15.50

In Table 2, we compare the computational costs between coarse NCM and MD simulations. We observe that the NCM simulation with $h=4a$ achieves a speedup[‡] of $15\times$ over MD.

Further comparisons between the MD and coarse NCM simulations are presented in Fig. 2. In (b), we compare the displacement profiles at the final time T , i.e., $u(x,T) = y(x,T) - x$, showing that the profile of the MD simulation is reproduced by the NCM simulations. In (c), we present the evolution of the kinetic energy (black lines), the potential/strain energy (blue lines), and the total energy (red lines) for the MD and coarse NCM simulations, showing the conservation of total energy in time on each simulation. As expected, fluctuations in the potential/strain energy have complementary fluctuations in the kinetic energy. Moreover, the kinetic, potential/strain, and total energy are preserved through the continuous upscaling process as shown in Fig. 2(c).

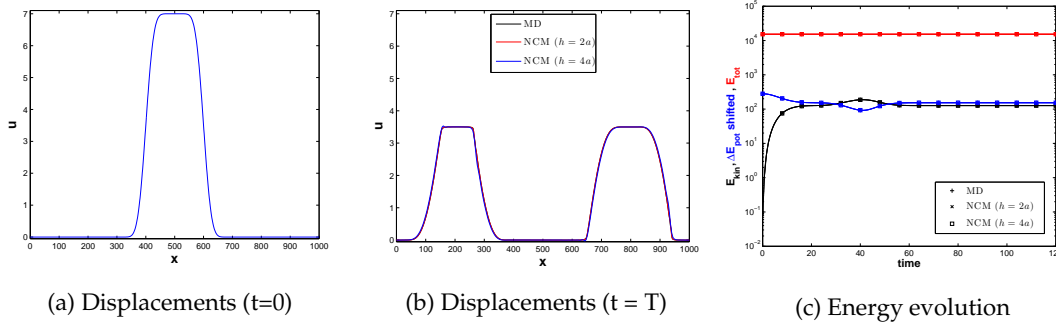


Figure 2: (a) Displacement profile assigned to the molecular dynamics (MD) embedded-atom model (2.3) and the upscaled nonlocal continuum model (NCM) (3.4) simulations, in the initial configuration. (b,c) Comparison between the MD and the coarse NCM simulations. The lattice constant in the MD simulation is denoted by a , and the mesh size in the NCM simulations is denoted by h . In (b), we compare the displacement profiles at the final time between the MD simulation and the coarse NCM simulations with mesh sizes of $h=2a$ and $h=4a$. A comparison of the energy evolution between the MD and the coarse NCM simulations is presented in (c). We plot the kinetic energy (black lines), the total energy (red lines), and the net change in potential/strain energy (blue lines) for each of the simulations. We shifted the net change in potential/strain energy by 280 for easier comparison to the change in kinetic energy.

[‡]The speedup is defined as the ratio of the total time of the MD simulation to the total time of the given simulation.

4 Continuous upscaling of a structured embedded-atom model

In Section 3, we showed the continuous upscaling of structureless MD EAMs. Here, we extend this technique to structured material models in higher dimensions.

In Section 4.1, we present an example of a structured MD model of the form of the EAM and derive its continuous upscaling to a NCM in Section 4.2. Numerical examples in Section 4.3 demonstrate that the upscaled continuum model reproduces the dynamics of the original MD model at greatly reduced cost.

In Section A.3.2, we show that our NCM (4.11) is an instance of a linear peridynamic solid model.

4.1 A structured embedded-atom model

Given a lattice \mathcal{L} , we define a monatomic crystal with atoms at positions $\mathbf{x}_i \in \mathcal{L} \cap \mathcal{B}$, $i = 1, \dots, N$, with \mathcal{B} a bounded body. We assume a homogeneous system[§] with potential energy

$$E_{\text{pot}} = \sum_i F(\rho_{h,i}) + \frac{1}{2} \sum_{\substack{i,j \\ (i \neq j)}} \phi_{ij}(r_{ij}). \quad (4.1)$$

The dependence of the embedding function on the host electron density is assumed of the form

$$F(\rho) = \frac{1}{2} c \left(\frac{\rho}{\rho_0} - 1 \right)^2, \quad (4.2)$$

where c is a constant and ρ_0 is the host electron density in the reference configuration. The host electron density evaluated at the location of the i -th atom is taken as

$$\rho_{h,i} = \sum_{j(\neq i)} f_{ij}(r_{ij}) \quad \text{with} \quad f_{ij}(r) = \chi_{ij}^\varepsilon f_0 \frac{v_a}{(r_{ij}^0)^{p-1}} r, \quad (4.3)$$

where $r_{ij}^0 := \|\mathbf{x}_j - \mathbf{x}_i\|$ and $r_{ij} := \|\mathbf{y}_j - \mathbf{y}_i\|$ are the distances between the i -th and j -th atoms in the reference and current configurations, respectively. The position of the i -th atom at time t is $\mathbf{y}_i = \mathbf{y}_i(t)$, \mathbf{x}_i is the reference position of the i -th atom, f_0 is a constant, v_a is the Wigner-Seitz cell of the crystal, p is a model parameter, and χ_{ij}^ε is defined as

$$\chi_{ij}^\varepsilon := \begin{cases} 1, & r_{ij}^0 \leq \varepsilon, \\ 0, & \text{otherwise,} \end{cases}$$

[§]The homogeneity of the system is expressed by introducing a single embedding function F for the entire system. In the standard EAM, the pair potential ϕ_{ij} may depend on the atom type i and atom type j . In contrast, the model (4.1) assumes a monatomic crystal. However, given atom i , the pair potential ϕ_{ij} may vary based on whether j is a nearest neighbor of atom i , a second nearest neighbor of atom i , etc. (see (4.5)).

where the parameter $\varepsilon > 0$ represents a horizon (*cf.* Section A.1.1). Note that in the reference configuration $r_{ij} = r_{ij}^0$, thus for an atom in the bulk of a homogeneous system

$$\rho_0 = \sum_{j \in \mathcal{F}_i} f_0 \frac{v_a}{(r_{ij}^0)^{p-2}} \quad (4.4)$$

with the *family* of the i -th atom defined as

$$\mathcal{F}_i := \left\{ j : \mathbf{x}_j \in \mathcal{B}; r_{ij}^0 \leq \varepsilon \right\}.$$

The pair potential is assumed to have the functional form

$$\phi_{ij}(r) = \frac{1}{2} \chi_{ij}^\varepsilon \frac{k}{(r_{ij}^0)^p} (r - r_{ij}^0)^2, \quad (4.5)$$

where k is a constant. The equation of motion for the i -th atom with mass m_i is (*cf.* (2.3))

$$m_i \frac{d^2 \mathbf{y}_i}{dt^2} = \sum_{j \in \mathcal{F}_i} \left\{ [F'(\rho_{h,i}) + F'(\rho_{h,j})] f'_{ij}(r_{ij}) + \phi'_{ij}(r_{ij}) \right\} \frac{\mathbf{y}_j - \mathbf{y}_i}{\|\mathbf{y}_j - \mathbf{y}_i\|} + \mathbf{f}_i^{\text{ext}}. \quad (4.6)$$

4.2 An upscaled structured embedded-atom model

In order to upscale (4.6), we take the potential energy density per particle (*cf.* (4.1))

$$e_i := \frac{1}{v_a} F(\rho_{h,i}) + \frac{1}{v_a} \frac{1}{2} \sum_{j \in \mathcal{F}_i} \phi_{ij}(r_{ij}) \quad (4.7)$$

as our QoI. As in Section 3.1, our goal is to derive an upscaled MD EAM which preserves this QoI under isotropic deformations, i.e., $r_{ij} = \chi r_{ij}^0, \forall i, j$ with χ a constant. We first derive the discrete coarse-grained model (4.9) below and then upscale it to a NCM. Starting with the first term on the right-hand side of (4.7) we have

$$\frac{1}{v_a} F(\rho_{h,i}) = \frac{1}{2} \frac{c}{v_a} \left(\frac{\rho_{h,i}}{\rho_0} - 1 \right)^2 \quad \text{with} \quad \frac{\rho_{h,i}}{\rho_0} = \frac{\sum_{j \in \mathcal{F}_i} f_0 \frac{v_a}{(r_{ij}^0)^{p-1}} r_{ij}}{\sum_{j \in \mathcal{F}_i} f_0 \frac{v_a}{(r_{ij}^0)^{p-2}}} = \frac{f_0 v_a \sum_{j \in \mathcal{F}_i} \frac{1}{(r_{ij}^0)^{p-2}} \chi}{f_0 v_a \sum_{j \in \mathcal{F}_i} \frac{1}{(r_{ij}^0)^{p-2}}} = \chi. \quad (4.8)$$

Under isotropic deformations, this term is preserved as long as $\bar{c} := c/v_a$ is kept constant. We thus express the embedding energy function as

$$F(\rho) = \frac{1}{2} \bar{c} v_a \left(\frac{\rho}{\rho_0} - 1 \right)^2.$$

The second term on the right-hand side of (4.7) can be written, for an isotropic deformation, as

$$\frac{1}{v_a} \frac{1}{2} \sum_{j \in \mathcal{F}_i} \phi_{ij}(r_{ij}) = \frac{1}{v_a} \frac{1}{2} \sum_{j \in \mathcal{F}_i} \frac{1}{2} \frac{k}{(r_{ij}^0)^p} (r_{ij} - r_{ij}^0)^2 = \frac{1}{4} \frac{k}{v_a} \sum_{j \in \mathcal{F}_i} \frac{1}{(r_{ij}^0)^{p-2}} (\chi - 1)^2 = \frac{1}{4} \bar{k} (\chi - 1)^2$$

with $\bar{k} := k\rho_0 / f_0 v_a^2$. This term is preserved under an isotropic deformation, provided that \bar{k} is kept constant. The pairwise potential is then expressed as

$$\phi_{ij}(r) = \frac{1}{2} \chi_{ij}^\varepsilon \frac{\bar{k} f_0}{\rho_0} \frac{v_a^2}{(r_{ij}^0)^p} (r - r_{ij}^0)^2.$$

Observing that

$$F'(\rho) = \frac{\bar{c}}{\rho_0} v_a \left(\frac{\rho}{\rho_0} - 1 \right), \quad f'_{ij}(r) = \chi_{ij}^\varepsilon f_0 \frac{v_a}{(r_{ij}^0)^{p-1}}, \quad \text{and} \quad \phi'_{ij}(r) = \chi_{ij}^\varepsilon \frac{\bar{k} f_0}{\rho_0} \frac{v_a^2}{(r_{ij}^0)^p} (r - r_{ij}^0),$$

the equation of motion (4.6) can be written as

$$m_i \frac{d^2 \mathbf{y}_i}{dt^2} = \sum_{j \in \mathcal{F}_i} \left\{ \left[\frac{\bar{c}}{\rho_0} \left(\frac{\rho_{h,i}}{\rho_0} - 1 \right) + \frac{\bar{c}}{\rho_0} \left(\frac{\rho_{h,j}}{\rho_0} - 1 \right) \right] \frac{f_0 v_a^2}{(r_{ij}^0)^{p-1}} + \frac{\bar{k} f_0}{\rho_0} \frac{v_a^2}{(r_{ij}^0)^p} (r_{ij} - r_{ij}^0) \right\} \times \frac{\mathbf{y}_j - \mathbf{y}_i}{\|\mathbf{y}_j - \mathbf{y}_i\|} + \mathbf{f}_i^{\text{ext}}, \quad (4.9)$$

which represents a coarse-grained model with two length scales: ε and $(v_a)^{1/3}$. The former is preserved in the upscaled NCM (4.11) below, whereas the latter represents a mesh size in the discretization of (4.11).

To proceed with the continuous upscaling of (4.9), let $\rho_i := m_i / v_a$ and $\mathbf{b}_i := \mathbf{f}_i^{\text{ext}} / v_a$. Then, divide (4.9) by v_a to get

$$\rho_i \frac{d^2 \mathbf{y}_i}{dt^2} = \sum_{j \in \mathcal{F}_i} \left\{ \left[\frac{\bar{c} f_0}{\rho_0} \left(\frac{\rho_{h,i}}{\rho_0} - 1 \right) + \frac{\bar{c} f_0}{\rho_0} \left(\frac{\rho_{h,j}}{\rho_0} - 1 \right) \right] \frac{1}{(r_{ij}^0)^{p-1}} + \frac{\bar{k} f_0}{\rho_0} \frac{1}{(r_{ij}^0)^p} (r_{ij} - r_{ij}^0) \right\} \times \frac{\mathbf{y}_j - \mathbf{y}_i}{\|\mathbf{y}_j - \mathbf{y}_i\|} v_a + \mathbf{b}_i. \quad (4.10)$$

Taking the summation in (4.10) as a quadrature of an integral, we obtain the upscaled EAM

$$\rho \frac{\partial^2 \mathbf{y}}{\partial t^2} = \int_{\mathcal{H}(\mathbf{x}, \varepsilon)} \left\{ \left[\frac{\bar{c} f_0}{\rho_0} \left(\frac{\rho_h}{\rho_0} - 1 \right) + \frac{\bar{c} f_0}{\rho_0} \left(\frac{\hat{\rho}_h}{\rho_0} - 1 \right) \right] \frac{1}{\|\hat{\mathbf{x}} - \mathbf{x}\|^{p-1}} + \frac{\bar{k} f_0}{\rho_0} \frac{1}{\|\hat{\mathbf{x}} - \mathbf{x}\|^p} (\|\hat{\mathbf{y}} - \mathbf{y}\| - \|\hat{\mathbf{x}} - \mathbf{x}\|) \right\} \times \frac{\hat{\mathbf{y}} - \mathbf{y}}{\|\hat{\mathbf{y}} - \mathbf{y}\|} dV_{\hat{\mathbf{x}}} + \mathbf{b}, \quad (4.11)$$

with $\rho = \rho(\mathbf{x})$, $\mathbf{y} := \mathbf{y}(\mathbf{x}, t)$, $\hat{\mathbf{y}} := \mathbf{y}(\hat{\mathbf{x}}, t)$, $\rho_h := \rho_h(\mathbf{x}, t)$, $\hat{\rho}_h := \rho_h(\hat{\mathbf{x}}, t)$, $\mathbf{b} = \mathbf{b}(\mathbf{x}, t)$, and where

$$\rho_{h,i} = \sum_{j \in \mathcal{F}_i} \frac{f_0 v_a}{(r_{ij}^0)^{p-1}} r_{ij} \approx f_0 \int_{\mathcal{H}(\mathbf{x}, \varepsilon)} \frac{1}{\|\hat{\mathbf{x}} - \mathbf{x}\|^{p-1}} \|\hat{\mathbf{y}} - \mathbf{y}\| dV_{\hat{\mathbf{x}}} =: \rho_h(\mathbf{x}, t) \quad (4.12)$$

with $\hat{\mathbf{y}} := \mathbf{y}(\hat{\mathbf{x}}, t)$. The integrations are over the neighborhood of \mathbf{x} (cf. (A.2)).

4.3 Numerical results

Let $\mathcal{B} = (-0.5, 0.5) \times (-0.5, 0.5)$ represent a two-dimensional plate and assume atoms are distributed on a square lattice with lattice constant a . We assume atoms interact through the EAM (4.6) with functions (4.2)-(4.5). A radially-symmetric initial configuration is chosen as follows: let $p(r)$ be a smooth 21-st order piecewise polynomial such that $p \equiv 0$ for $r \geq 0.2$, $p(0) = 1e - 4$, and $p'(r) = p''(r) = \dots = p^{(10)}(r) = 0$ for $r = 0, 0.2$. Given an atom with lattice position \mathbf{x} , its initial position is given by $\mathbf{y} = \mathbf{x} + p(r)\hat{\mathbf{r}}$ with \mathbf{r} its position vector relative to the center of the plate, $r := \|\mathbf{r}\|$, and $\hat{\mathbf{r}} := \mathbf{r}/r$; see Fig. 3. The system is evolved in time using the velocity-Verlet algorithm with timestep Δt_0 and final time T . We compare the results of the MD simulation to NCM simulations using (4.11). We discretize the NCM using square lattices with mesh sizes of $h = a, 2a, 4a$ in PDLAMMPS [23–25]. The initial configuration in the NCM simulations is the same as in the MD simulation, and the time step in the discretized NCMs is adapted with the spatial discretization so that $\Delta t = \Delta t_0 h/a$. We assume no external forces, i.e., $\mathbf{f}_i^{\text{ext}} \equiv \mathbf{0}$ in (4.6) and $\mathbf{b} \equiv \mathbf{0}$ in (4.11). The parameters used for the simulations are described in Table 3.

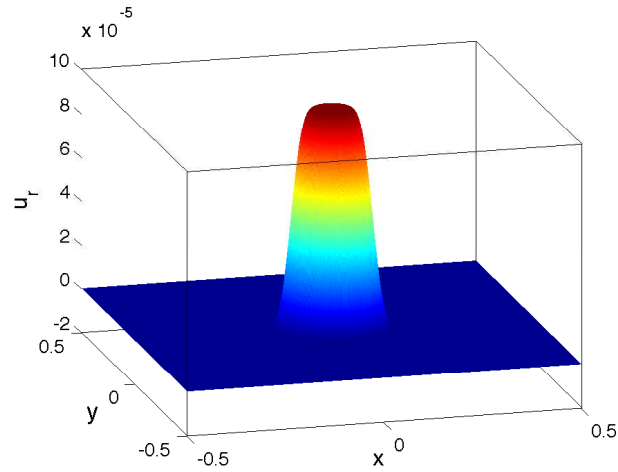


Figure 3: Radial displacement profile assigned to the initial configuration for the two-dimensional simulations in Fig. 4. Each point is displaced relative to its reference position an amount of $u_r = p(r)$ radially with respect to the center of the plate with $p(r)$ a smooth 21-st order piecewise polynomial.

Table 3: Parameters for the structured MD EAM and upscaled NCM simulations (*cf.* (4.10)).

ρ	\bar{k}	\bar{c}	f_0/ρ_0	a	ε	Δt_0	T	p
8,960	$1.44e12$	$5.4e11$	1	$1.25e-3$	$12a$	$1.25e-9$	$2.5e-5$	1

In Fig. 4, we compare the MD potential energy (a) and NCM strain energy (b,c,d), for different mesh sizes, at the final time T . In Fig. 5(a), we compare the radial displacements with respect to the center of the plate, at the final time T , for atoms/particles with reference position along the x -axis. We observe that the dynamics of the MD system are preserved, up to discretization errors, by the coarse NCM simulations with mesh sizes of $h = 2a, 4a$, at greatly reduced cost, as shown in the computational cost comparison between the MD and the coarse NCM simulations in Table 4. The NCM simulation with $h = 4a$ achieves a speedup of about 1,000 and a reduction of memory usage per processor

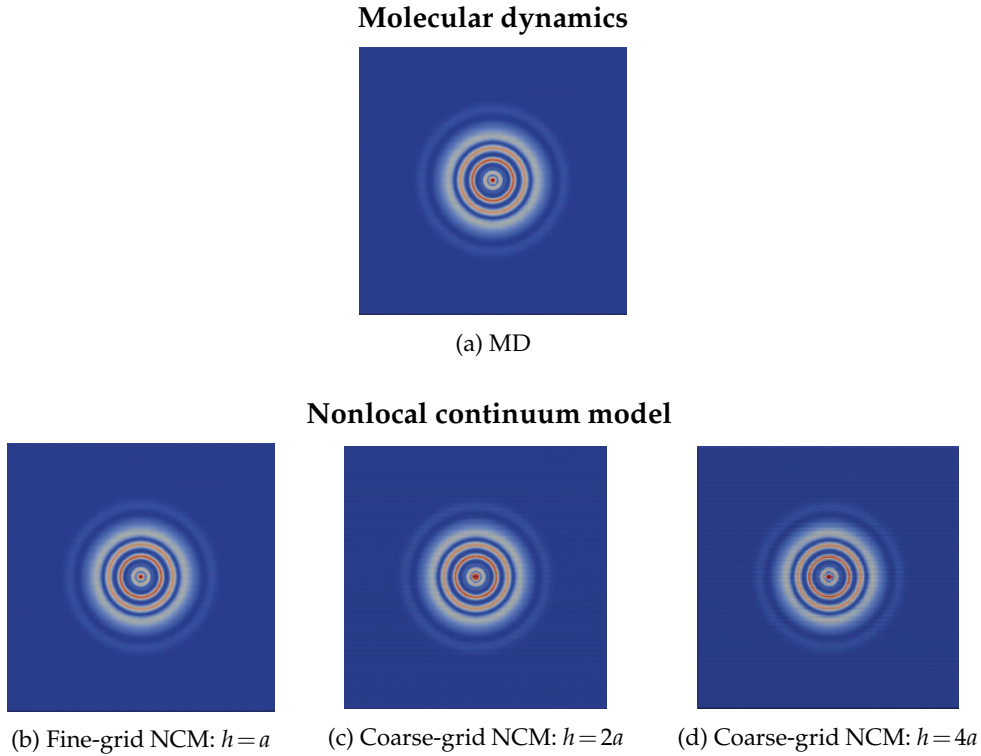


Figure 4: Molecular dynamics (MD) potential energy (a) and nonlocal continuum model (NCM) strain energy (b,c,d) profile for two-dimensional wave propagation on a plate. We compare (a) an MD simulation for the EAM (4.6) with functions (4.2)-(4.5) on a square lattice with lattice constant a and (b,c,d) NCM simulations using (4.11) discretized using square lattices with mesh sizes of (b) $h = a$, (c) $h = 2a$, and (d) $h = 4a$. The radial displacement profile assigned to the reference positions in the initial configuration is presented in Fig. 3. The figures show the potential energy (MD)/strain energy (NCM) profile at the final time. The simulation parameters are presented in Table 3. The largest energy value is indicated by red and the smallest one by blue.

Table 4: Comparison between the computational cost of the molecular dynamics (MD) simulation and the coarse nonlocal continuum model (NCM) simulations presented in Fig. 4. The lattice constant in the MD simulation is denoted by a , and the mesh size in the NCM simulations is denoted by h . A significant reduction in degrees of freedom (number of particles and bonds) as well as in memory usage and simulation time is shown.

	MD	NCM ($h=2a$)	NCM ($h=4a$)
Number of atoms/particles	640,000	160,000	40,000
Number of bonds	296,960,000	17,920,000	1,120,000
Memory usage per processor (Mbytes)	151.63	19.92	7.33
Total time (seconds)	14,564.30	446.45	14.48
Speedup	1	32.62	1,005.82

of about 95%. All computations were run on 64 cores of Sandia's Red Sky supercomputer. In Fig. 5(b), a comparison of the kinetic energy (black lines), the potential/strain energy (blue lines), and the total energy (red lines) between the MD and coarse NCM simulations is presented, showing the conservation of total energy in time for each simulation. As expected, fluctuations in the potential/strain energy have complementary fluctuations in the kinetic energy. Moreover, we observe that the kinetic, potential/strain, and total energy are preserved through the continuous upscaling process.

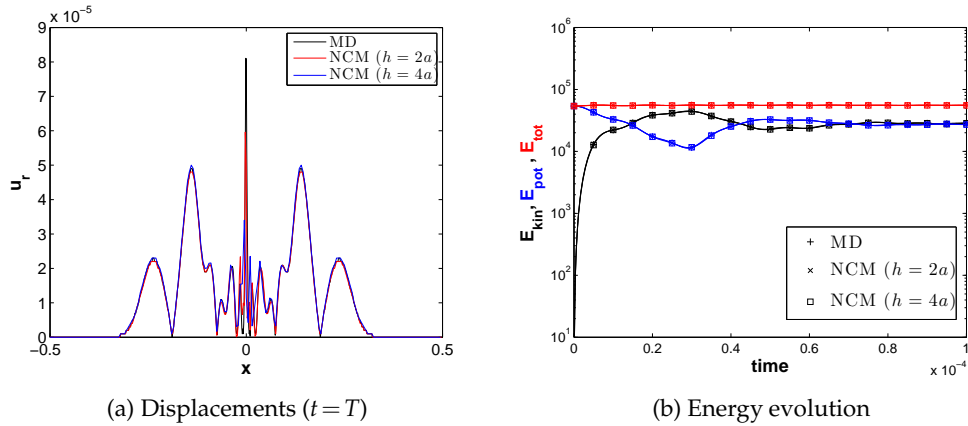


Figure 5: (a) Radial displacements, with respect to the center of the plate, in the simulations presented in Fig. 4 at the final time, for atoms/particles with reference positions along the x -axis. We compare the results of a molecular dynamics (MD) simulation with lattice constant a and coarse nonlocal continuum model (NCM) simulations with mesh sizes of $h=2a$, $4a$. (b) Comparison of the energy evolution between the MD and the coarse NCM simulations. We plot the kinetic energy (black lines), the potential/strain energy (blue lines), and the total energy (red lines) for each of the simulations.

The simulations presented in Fig. 4 show that significant savings in simulation time and memory usage can be obtained through continuous upscaling. Of particular interest are scenarios where fine-scale simulations are unfeasible, requiring the use of models with a reduced number of degrees of freedom. To demonstrate this situation, we perform a three-dimensional simulation on a cubic domain $\mathcal{B} = (-0.5, 0.5) \times (-0.5, 0.5) \times (-0.5, 0.5)$. We simulate a radial wave propagation in a system described by the NCM

(4.11) with $\bar{k} = 2.28e12$, $\bar{c} = 4.8e11$, uniform mass density $\rho = 8908$ (values corresponding to Ni), $f_0/\rho_0 = 1$, and $p = 1$. The system is discretized using a cubic lattice with mesh size $h = 5e-3$ in PDLAMMPS with a total of 8,040,000 particles. We choose a horizon of $\varepsilon = 3h$. A spherically-symmetric initial configuration is chosen, in complete analogy to the initial configuration in the two-dimensional simulations in Fig. 4. The system is evolved in time using the velocity-Verlet algorithm with timestep $\Delta t = 5e-9$ and final time $T = 5e-5$, with 4,096 cores on Sandia's Red Sky supercomputer. We assume no external forces, i.e., $\mathbf{b} \equiv \mathbf{0}$. The strain energy at the final time T is presented in Fig. 6 on an octant of the entire cube to illustrate the wave propagation along the three dimensions.

Although we have performed fine-scale simulations for the 1D and 2D models presented thus far, a fine-scale simulation for this 3D model vastly exceeds our computational resources. This serves to demonstrate the value of continuous upscaling, especially for 3D models. A fine-scale 3D atomistic simulation, with a lattice constant of $a = h/4$, where h is the grid size used for the upscaled calculation of Fig. 6, would have about 512,000,000 atoms. Assuming $\varepsilon = 12a$ and a timestep of $\Delta t_0 = \Delta t/4$, an equivalent fine-scale simulation would roughly incur a simulation time 16,000 times larger than the coarse NCM simulation; i.e., a simulation in NCM taking about an hour would correspond to a two-year fine-scale simulation. Furthermore, the amount of memory required just to store the information for the bonds in the fine-scale simulation is estimated about 10 TB.

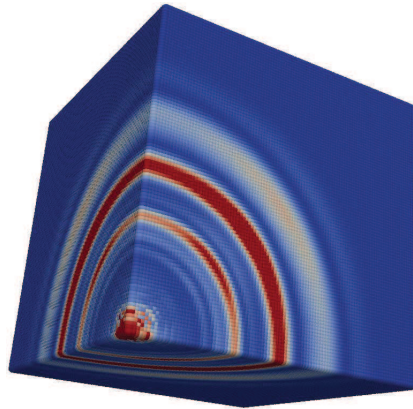


Figure 6: An octant of a three-dimensional wave propagation simulation on a cubic domain with the NCM (4.11), having a spherically-symmetric initial condition. The NCM strain energy at the final time is shown, where the largest value is indicated by red and the smallest one by blue.

5 Concluding remarks

We presented a model reduction technique for multibody molecular dynamics (MD) potentials of the form of the embedded-atom model (EAM), using a continuous upscaling to nonlocal continuum models (NCMs). This technique provides a means to upscale

MD EAM simulations at greatly reduced cost. We demonstrated the continuous upscaling analytically and numerically with examples of structured and structureless material models.

In Appendix A, we demonstrate that the NCMs used for upscaling MD EAMs are instances of the state-based peridynamics (PD) theory of solid mechanics. This theory provides a general framework for nonlocal continuum models. By establishing relationships between multibody or volume-dependent interaction PD models and theories, we obtain the taxonomy presented in Fig. 7. This taxonomy shows that multibody potentials of the form of the MD EAM can be represented within the state-based PD theory, through the EAM-like PD model.

The EAM-like PD model was originally proposed as an extension of the bond-based PD theory. This represented a first attempt to derive multibody potentials in PD capable of modeling materials with a general Poisson's ratio, as the original bond-based PD theory was only capable of modeling materials with a Poisson's ratio of $\nu = 1/4$ (in 3D). The state-based PD theory was introduced later as a general theory also capable of representing materials with a general Poisson's ratio. Since then, the original EAM-like PD model has largely been forgotten by the PD community. We show that this model is more fundamental than more recently developed and commonly used state-based constitutive models, and is also essential in the upscaling of MD models of the form of the EAM. This suggests that the original EAM-like PD model is worth revisiting.

Acknowledgments

The research at Florida State University was supported by the Department of Energy grant number DE-SC0004970 and the National Science Foundation under grant number DMS-1013845, at the University of Texas by the Department of Energy grant number DE-FG02-05ER25701, and by the Laboratory Directed Research and Development program at Sandia National Laboratories. The authors acknowledge helpful discussions with Stephen Foiles as well as valuable encouragement and suggestions of Richard Lehoucq from Sandia National Laboratories. The first author, Pablo Seleson, is also thankful for the support from the ICES Postdoctoral Fellowship Program.

Appendix A: Peridynamics for upscaled nonlocal continuum models

The peridynamics (PD) theory of solid mechanics is a nonlocal continuum theory with deep natural connections to molecular dynamics (MD). Although it is a *continuum* theory, it possesses some properties inherent to *discrete* MD models. In particular, as in MD, PD constitutive models include both pairwise and multibody potentials. Likewise, pair potentials in PD exhibit certain limitations which are removed by the introduction of multibody potentials. Due to similarities in the way internal forces are calculated in both

models, PD has been called a “continuum” formulation of MD [8]. Particularly, a certain discretization of PD has the same computational structure as MD, which allows for the implementation of PD models in MD software [24].

In contrast to classical continuum mechanics, PD possesses a length scale that may be chosen to match the dominant length scale of the system of interest, making it suitable for multiscale modeling [26]. See [27] for a multiscale PD model of fiber-reinforced composites. PD has also been applied to concurrent multiscale modeling at the discrete level in [28,29] and at the continuum level in [30–32].

We survey PD theories and relevant models in Section A.1 and establish a partial taxonomy in Section A.2, illustrated in Fig. 7. In Section A.3, we demonstrate that all the nonlocal continuum models (NCMs) derived in this paper are PD models, showing a deep connection between the MD embedded-atom model (EAM) and PD. This provides support for the claim that PD is a mathematical theory that unifies the mechanics of particles and continua.

A.1 Peridynamic theories and models

PD was proposed in [8] as a nonlocal extension of classical continuum solid mechanics. PD is a nonlocal theory, based upon an integro-differential formulation that eliminates the spatial differentiability requirement for displacement fields usually assumed in classical continuum mechanics. This makes the PD theory suitable for modeling fracture [33]. A consequence of this integro-differential formulation is that material points separated by a finite distance interact directly with each other. Earlier NCMs in mechanics can be found in [34–38].

A.1.1 Peridynamic theories: state-based and bond-based

We discuss two formulations of PD, the *state-based* theory and the *bond-based* theory. Energy conserving state-based models are associated with *multibody* potentials, whereas energy conserving bond-based models are associated with *pair* potentials. The bond-based PD theory is a special case of the state-based theory, as explained below.

In the most general formulation of PD, the state-based PD theory [9], the equation of motion for a point \mathbf{x} within a bounded body \mathcal{B} at time $t > 0$ is

$$\rho(\mathbf{x}) \frac{\partial^2 \mathbf{u}}{\partial t^2}(\mathbf{x}, t) = \int_{\mathcal{B}} \{ \underline{\mathbf{T}}[\mathbf{x}, t](\zeta) - \underline{\mathbf{T}}[\hat{\mathbf{x}}, t](\langle -\zeta \rangle) \} dV_{\hat{\mathbf{x}}} + \mathbf{b}(\mathbf{x}, t), \quad (\text{A.1})$$

where ρ denotes the mass density, \mathbf{u} the displacement field, \mathbf{b} an external body force density, and the operator $\underline{\mathbf{T}}$ the *force vector state*. In the standard PD notation, given two material points $\hat{\mathbf{x}}$ and \mathbf{x} , we denote their relative position in the reference configuration and their relative displacement in the current configuration by $\zeta := \hat{\mathbf{x}} - \mathbf{x}$ and $\eta := \mathbf{u}(\hat{\mathbf{x}}, t) - \mathbf{u}(\mathbf{x}, t)$, respectively. Notice that $\zeta + \eta$ is their relative position in the current configuration. A *state* is an operator, denoted by an underscored symbol, that operates on vectors defined by the *bonds* ζ that define an interaction between each pair of points

$\hat{\mathbf{x}}$ and \mathbf{x} in \mathcal{B} . A *vector state* operator is a generalization of a second-order tensor and maps each bond to a vector. A *scalar state* operator maps each bond to a scalar. A state can be defined at a particular point in space and time. This is specified by arguments in square brackets, i.e., $[\mathbf{x}, t]$. For further details regarding states, see [9]. The first term on the right-hand side of (A.1) is analogous to the divergence of a stress tensor as in classical continuum mechanics [39,40]. In PD, a point \mathbf{x} interacts directly only with points $\hat{\mathbf{x}}$ within its *neighborhood* $\mathcal{H}(\mathbf{x}, \varepsilon)$ defined as

$$\mathcal{H}(\mathbf{x}, \varepsilon) := \{\hat{\mathbf{x}} \in \mathcal{B} : \|\hat{\mathbf{x}} - \mathbf{x}\| \leq \varepsilon\}, \quad (\text{A.2})$$

so that $\underline{\mathbf{T}}[\mathbf{x}, t] \langle \boldsymbol{\zeta} \rangle = \mathbf{0}$ for $\|\boldsymbol{\zeta}\| > \varepsilon$, where $\|\cdot\|$ denotes the Euclidean norm. The parameter $\varepsilon > 0$ is called the *horizon* and is analogous to a cutoff radius in MD.

A particular class of force vector states known as *ordinary materials* is written as

$$\underline{\mathbf{T}}[\mathbf{x}, t] \langle \boldsymbol{\zeta} \rangle = \underline{t}[\mathbf{x}, t] \langle \boldsymbol{\zeta} \rangle \frac{\boldsymbol{\zeta} + \boldsymbol{\eta}}{\|\boldsymbol{\zeta} + \boldsymbol{\eta}\|}, \quad (\text{A.3})$$

for $\|\boldsymbol{\zeta} + \boldsymbol{\eta}\| \neq 0$ and $\mathbf{0}$ otherwise, with \underline{t} a *force scalar state*. For this class of force vector states, balance of linear and angular momenta are satisfied for any bounded body \mathcal{B} [9, Propositions 7.1 and 8.2]. Conditions for which more general force vector states satisfy balance of linear and angular momenta are given in [9].

For the case where the nonlocal interactions derive from pair potentials, the force scalar state can be expressed as

$$\underline{t}[\mathbf{x}, t] \langle \boldsymbol{\zeta} \rangle = \frac{1}{2} \kappa(\boldsymbol{\eta}, \boldsymbol{\zeta}) \quad (\text{A.4})$$

with κ the *pairwise force scalar function* satisfying $\kappa(\boldsymbol{\eta}, \boldsymbol{\zeta}) = \kappa(-\boldsymbol{\eta}, -\boldsymbol{\zeta})$ [9]. Then, (A.1) reduces to

$$\rho(\mathbf{x}) \frac{\partial^2 \mathbf{u}}{\partial t^2}(\mathbf{x}, t) = \int_{\mathcal{B}} \kappa(\boldsymbol{\eta}, \boldsymbol{\zeta}) \frac{\boldsymbol{\zeta} + \boldsymbol{\eta}}{\|\boldsymbol{\zeta} + \boldsymbol{\eta}\|} dV_{\hat{\mathbf{x}}} + \mathbf{b}(\mathbf{x}, t), \quad (\text{A.5})$$

the equation of motion for the bond-based PD theory presented in [8].

Remark A.1. The particular choice of force scalar state (A.4), leading to the equation of motion (A.5), demonstrates that the bond-based PD theory is a special case of the state-based PD theory, as explained in [9].

A.1.2 State-based peridynamic models

We review some state-based PD models here and present their connections in Section A.2.

Linear peridynamic solid model. A commonly used state-based constitutive model is the *linear peridynamic solid* (LPS) model [9], a nonlocal analogue to a linear isotropic elastic material. It is an ordinary material with force scalar state

$$\underline{t} = \frac{3K\theta}{m} \underline{\omega x} + \alpha \underline{\omega e^d}, \quad (\text{A.6})$$

where $\underline{\omega}$ denotes an *influence function* [9, Definition 3.2]. Influence functions are nonnegative scalar states defined on $\mathcal{H}(\mathbf{x}, \varepsilon)$. A *spherical influence function* depends only upon $\|\boldsymbol{\zeta}\|$, i.e., $\underline{\omega}(\boldsymbol{\zeta}) = \tilde{\omega}(\|\boldsymbol{\zeta}\|)$. Let \underline{x} be the *reference relative distance scalar state*, i.e., $\underline{x}(\boldsymbol{\zeta}) := \|\boldsymbol{\zeta}\|$, and m be the *weighted volume*, defined as

$$m := \int_{\mathcal{B}} \underline{\omega}(\boldsymbol{\zeta}) \underline{x}(\boldsymbol{\zeta}) \underline{x}(\boldsymbol{\zeta}) dV_{\hat{\mathbf{x}}}. \quad (\text{A.7})$$

We define the *dilatation*

$$\theta[\mathbf{x}, t] := \frac{3}{m} \int_{\mathcal{B}} \underline{\omega}(\boldsymbol{\zeta}) \underline{x}(\boldsymbol{\zeta}) \underline{e}[\mathbf{x}, t](\boldsymbol{\zeta}) dV_{\hat{\mathbf{x}}},$$

where \underline{e} is the *extension scalar state*

$$\underline{e}[\mathbf{x}, t](\boldsymbol{\zeta}) := \|\boldsymbol{\zeta} + \boldsymbol{\eta}\| - \|\boldsymbol{\zeta}\|. \quad (\text{A.8})$$

The *isotropic* and *deviatoric* parts of the extension scalar state are defined, respectively, as

$$\underline{e}^i := \frac{\theta \underline{x}}{3} \quad \text{and} \quad \underline{e}^d := \underline{e} - \underline{e}^i.$$

For a spherical influence function, the LPS model is isotropic [9, Proposition 15.1]. In this model, K is the bulk modulus and $\alpha = 15G/m$, with G the shear modulus.

EAM-like PD model. A generalization of the bond-based PD theory was proposed in [8], before the state-based PD theory was formulated. It represented a first attempt to derive multibody interaction models in PD that allow for general Poisson's ratios, as opposed to bond-based PD models which are restricted to a Poisson's ratio of $\nu = 1/4$ (in 3D). The basic idea was to modify the macroelastic energy density W of the bond-based PD theory to include a volumetric term. The modified macroelastic energy density takes the form

$$\widehat{W}(\mathbf{x}, t) = E(\vartheta(\mathbf{x}, t)) + W(\mathbf{x}, t).$$

Here, W is a bond-based macroelastic energy density based on pair potentials, and is given by

$$W(\mathbf{x}, t) := \frac{1}{2} \int_{\mathcal{B}} w(\boldsymbol{\eta}, \boldsymbol{\zeta}) dV_{\hat{\mathbf{x}}} \quad (\text{A.9})$$

with w a pairwise potential function. E is a volume-dependent strain energy term. The function

$$\vartheta(\mathbf{x}, t) := \int_{\mathcal{B}} j(\|\boldsymbol{\zeta}\|) \|\boldsymbol{\zeta} + \boldsymbol{\eta}\| dV_{\hat{\mathbf{x}}} \quad (\text{A.10})$$

is a weighted average in the current configuration of the lengths of all the bonds belonging to the point \mathbf{x} , with j a scalar-valued spherical weighting function. Because of the

similarities between this model and the MD EAM (cf. Section 2), we refer to this model as the *EAM-like PD model*.[¶]

By Hamilton's principle, the equation of motion for the EAM-like PD model is obtained (cf. [8]), giving for $\mathbf{x} \in \mathcal{B}$ and $t > 0$,

$$\rho(\mathbf{x}) \frac{\partial^2 \mathbf{u}}{\partial t^2}(\mathbf{x}, t) = \int_{\mathcal{B}} \left\{ - (P(\mathbf{x}, t) + P(\hat{\mathbf{x}}, t)) j(\|\boldsymbol{\xi}\|) + \kappa(\boldsymbol{\eta}, \boldsymbol{\xi}) \right\} \frac{\boldsymbol{\xi} + \boldsymbol{\eta}}{\|\boldsymbol{\xi} + \boldsymbol{\eta}\|} dV_{\hat{\mathbf{x}}} + \mathbf{b}(\mathbf{x}, t), \quad (\text{A.11})$$

where

$$P(\mathbf{x}, t) := -E'(\vartheta(\mathbf{x}, t)) \quad \text{and} \quad \frac{\partial w}{\partial \boldsymbol{\eta}}(\boldsymbol{\eta}, \boldsymbol{\xi}) = \kappa(\boldsymbol{\eta}, \boldsymbol{\xi}) \frac{\boldsymbol{\xi} + \boldsymbol{\eta}}{\|\boldsymbol{\xi} + \boldsymbol{\eta}\|}. \quad (\text{A.12})$$

We denote by E' the derivative of E with respect to its argument ϑ . By comparing (A.11) with (A.5), we observe that the interaction between PD material points was generalized to include a volume-dependent term. Unlike the bond-based PD theory, bonds here are not independent.

A.2 Relationships between models and theories in state-based peridynamics

As discussed in Section A.1, the state-based PD theory is the most general PD framework. However, the EAM-like PD model was proposed well before the state-based PD theory. Here, we study the connections between the EAM-like PD model and the state-based PD theory, investigating specifically the relation between the EAM-like PD model and the LPS constitutive model.

A.2.1 State-based formulation for the EAM-like PD model

We show that the EAM-like PD model (A.11) is an instance of the state-based PD theory (A.1). For that purpose, we choose an ordinary material with force scalar state

$$\underline{t}[\mathbf{x}, t] \langle \boldsymbol{\xi} \rangle = -P(\mathbf{x}, t) j(\|\boldsymbol{\xi}\|) + \frac{1}{2} \kappa(\boldsymbol{\eta}, \boldsymbol{\xi}), \quad (\text{A.13})$$

for which the equation of motion (A.1) gives (A.11). Inspection of the form of (A.13) reveals that it cannot be further reduced to the form (A.4), and thus it is not a bond-based PD material.

Remark A.2. The EAM-like PD model represents an ordinary state-based PD material with force scalar state (A.13).

[¶]We observe that the EAM-like PD model is not, strictly speaking, a constitutive model. The reason is that the functional form of the pairwise potential function w and the volume-dependent strain energy E (which depends on the deformation) need to be specified. However, due to the fact that it represents a particular class of multibody potentials (of similar structure to the MD EAM), we do not refer to it as a theory per se.

A.2.2 Peridynamic constitutive models based upon the EAM-like PD model

We now demonstrate that the LPS model (A.6) is an instance of the EAM-like PD model by choosing a particular P , j , and κ in (A.13). Assume the pairwise force scalar function

$$\kappa(\boldsymbol{\eta}, \boldsymbol{\xi}) = \frac{30G}{\hat{m}} j(\|\boldsymbol{\xi}\|) s(\boldsymbol{\eta}, \boldsymbol{\xi}) \quad (\text{A.14})$$

with G the shear modulus. The pairwise stretch function s and the scalar \hat{m} are defined as

$$s(\boldsymbol{\eta}, \boldsymbol{\xi}) := \frac{\|\boldsymbol{\xi} + \boldsymbol{\eta}\| - \|\boldsymbol{\xi}\|}{\|\boldsymbol{\xi}\|}, \quad \hat{m} := \int_{\mathcal{B}} j(\|\boldsymbol{\xi}\|) \|\boldsymbol{\xi}\| dV_{\hat{\mathbf{x}}}.$$

Let the scalar-valued spherical weighting function j be given by

$$j(\|\boldsymbol{\xi}\|) = \underline{\omega}\langle \boldsymbol{\xi} \rangle \|\boldsymbol{\xi}\|, \quad (\text{A.15})$$

with $\underline{\omega}\langle \boldsymbol{\xi} \rangle$ a spherical influence function. Then, $\hat{m} = m$, the weighted volume (A.7) of the state-based PD theory. Let ϑ_0 denote the evaluation of $\vartheta(\mathbf{x}, t)$ (cf. (A.10)) in the reference configuration, i.e. $\boldsymbol{\eta} \equiv \mathbf{0}$. Then, $\hat{m} = \vartheta_0$. We can thus refer to $\vartheta(\mathbf{x}, t)$ as the *weighted deformed volume* corresponding to the point \mathbf{x} in the deformed configuration at time t . We can now write the pairwise force scalar function κ in (A.14) as

$$\kappa(\boldsymbol{\eta}, \boldsymbol{\xi}) = \frac{30G}{m} \underline{\omega}\langle \boldsymbol{\xi} \rangle \underline{e}[\mathbf{x}, t]\langle \boldsymbol{\xi} \rangle,$$

with \underline{e} the extension scalar state (cf. (A.8)). Further, assume a volume-dependent strain energy

$$E(\vartheta) = \frac{3K-5G}{m} \left(\frac{3}{m} \frac{\vartheta^2}{2} - 3\vartheta + C \right) \quad (\text{A.16})$$

with C an arbitrary constant independent of ϑ . Then, by (A.12), we have

$$P(\mathbf{x}, t) = -\frac{3K-5G}{m} \left(\frac{3}{m} \vartheta(\mathbf{x}, t) - 3 \right).$$

We observe that

$$\frac{3}{m} \vartheta(\mathbf{x}, t) - 3 = \theta[\mathbf{x}, t], \quad (\text{A.17})$$

so that

$$P(\mathbf{x}, t) = -\frac{3K-5G}{m} \theta[\mathbf{x}, t].$$

The force scalar state (A.13) can thus be written as

$$\underline{t}[\mathbf{x}, t]\langle \boldsymbol{\xi} \rangle = \frac{3K\theta[\mathbf{x}, t]}{m} \underline{\omega}\langle \boldsymbol{\xi} \rangle \underline{x}\langle \boldsymbol{\xi} \rangle + \alpha \underline{\omega}\langle \boldsymbol{\xi} \rangle \underline{e}^d[\mathbf{x}, t]\langle \boldsymbol{\xi} \rangle,$$

the LPS force scalar state (A.6). The derivations are straightforward and left to the reader.

Remark A.3. We have shown that the LPS model presented in Section A.1.2 is an instance of the EAM-like PD model, which is itself a state-based PD model (*cf.* Section A.2.1). The LPS model can be derived from the EAM-like PD model by assuming (A.14)-(A.16).

In [41], it was shown that by assuming a Poisson’s ratio $\nu = 1/4$ and the particular influence function $\underline{\omega}(\boldsymbol{\zeta}) = \|\boldsymbol{\zeta}\|^{-1}$, i.e., $j(\|\boldsymbol{\zeta}\|) \equiv 1$ in (A.15), the prototype microelastic brittle (PMB) model [33] can be derived from the LPS model (A.6), demonstrating that influence functions may be used to connect various PD constitutive models. For more on the role of the influence function in PD, see [41]. These relations establish a partial taxonomy of PD constitutive model classes, represented in Fig. 7. A connection between the EAM-like PD model and the MD EAM is derived in Section A.3 and is also indicated in Fig. 7.

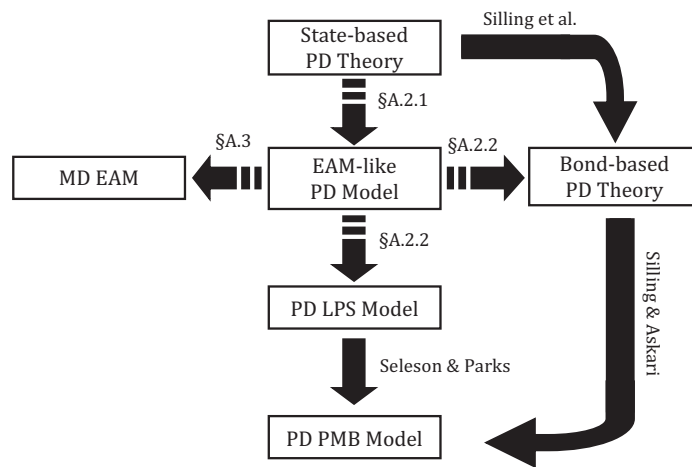


Figure 7: Relationships between theories and models in peridynamics (PD). In Silling et al. [9], it was shown that the bond-based PD theory is a special case of the state-based PD theory. A generalization of the bond-based PD theory with similar structure to the molecular dynamics (MD) embedded-atom model (EAM) was proposed in [8]; we therefore call it *EAM-like PD model*. In Section A.2.1, it is shown that the EAM-like PD model is an instance of the state-based PD theory. Common PD constitutive models are shown to be special cases of the EAM-like PD model as follows. In Section A.2.2, the state-based linear peridynamic solid (LPS) model [9] is derived from the EAM-like PD model. Furthermore, in Seleson & Parks [41], the bond-based prototype microelastic brittle (PMB) model presented in Silling & Askari [33] is derived from the LPS model. This establishes a partial taxonomy of PD models and theories. The EAM-like PD model (A.11) gives the bond-based PD theory for $P(\mathbf{x}, t) \equiv 0$. An example is described in Remark A.5 for a Poisson’s ratio of $\nu = 1/4$ using (A.16). In addition, in Section A.3 it is shown that the EAM-like PD model can be connected to the MD EAM.

Remark A.4. The derivations connecting the LPS model (A.6) and the EAM-like PD model (A.13) establish a useful relationship between two characteristic volume-dependent variables: the dilatation θ and the weighted deformed volume ϑ (*cf.* (A.17)), i.e.,

$$\theta[\mathbf{x}, t] = 3 \left(\frac{\vartheta(\mathbf{x}, t)}{\vartheta_0} - 1 \right). \tag{A.18}$$

Remark A.5. Let an EAM-like PD model be defined by the volume-dependent strain energy $E(\vartheta)$ given in (A.16) (i.e., the one related to the LPS model) and assume an arbitrary pairwise force scalar function $\kappa(\boldsymbol{\eta}, \boldsymbol{\xi})$. We assume a Poisson's ratio of $\nu = 1/4$, for which case the relation $5G = 3K$ holds and thus $P(\mathbf{x}, t) = 0$. As a consequence, the volume-dependent term vanishes in (A.11) and we recover the bond-based PD theory (A.5).

A.3 Continuous upscaling to peridynamic models

In this section we show that the NCMs (3.4) and (4.11) are instances of PD models.

A.3.1 Structureless MD EAM

We demonstrate the connection between (3.4) and an EAM-like PD model. For that purpose, we generalize (A.11) to allow the description of structureless materials. Let a generalized weighted deformed volume (cf. (A.10)) be^{||}

$$\vartheta(\mathbf{x}, t) := \int_B j(\boldsymbol{\eta}, \boldsymbol{\xi}) dV_{\hat{\mathbf{x}}} \quad (\text{A.19})$$

with j a scalar-valued function and $\boldsymbol{\xi}, \boldsymbol{\eta}$ defined in Section A.1.1. Assuming the conditions

$$\frac{\partial w}{\partial \boldsymbol{\eta}}(-\boldsymbol{\eta}, -\boldsymbol{\xi}) = -\frac{\partial w}{\partial \boldsymbol{\eta}}(\boldsymbol{\eta}, \boldsymbol{\xi}) \quad \text{and} \quad \frac{\partial j}{\partial \boldsymbol{\eta}}(-\boldsymbol{\eta}, -\boldsymbol{\xi}) = -\frac{\partial j}{\partial \boldsymbol{\eta}}(\boldsymbol{\eta}, \boldsymbol{\xi}) \quad (\text{A.20})$$

are satisfied, the equation of motion corresponding to the generalized EAM-like PD model with (A.19) can be written as (cf. (A.11))

$$\rho(\mathbf{x}) \frac{\partial^2 \mathbf{u}}{\partial t^2}(\mathbf{x}, t) = \int_B \left[-(P(\mathbf{x}, t) + P(\hat{\mathbf{x}}, t)) \frac{\partial j}{\partial \boldsymbol{\eta}}(\boldsymbol{\eta}, \boldsymbol{\xi}) + \frac{\partial w}{\partial \boldsymbol{\eta}}(\boldsymbol{\eta}, \boldsymbol{\xi}) \right] dV_{\hat{\mathbf{x}}} + \mathbf{b}(\mathbf{x}, t). \quad (\text{A.21})$$

Remark A.6. We observe that (A.19) generalizes (A.10) in that the explicit dependence upon $\|\boldsymbol{\xi}\|$ has been removed.

We now make particular choices for the components in (A.21)**:

$$j(\boldsymbol{\eta}, \boldsymbol{\xi}) = \sum_{\substack{n_1, n_2, n_3 \\ \mathbf{n} \neq \mathbf{0}}} f(\|\boldsymbol{\xi} + \boldsymbol{\eta}\|) \delta^{(3)} \left(\boldsymbol{\xi} - \frac{n_i \mathbf{a}_i^0}{\sigma r_{1e}^0} \boldsymbol{\mu} \right), \quad (\text{A.22})$$

$$w(\boldsymbol{\eta}, \boldsymbol{\xi}) = \sum_{\substack{n_1, n_2, n_3 \\ \mathbf{n} \neq \mathbf{0}}} \bar{\varphi}(\|\boldsymbol{\xi} + \boldsymbol{\eta}\|) \delta^{(3)} \left(\boldsymbol{\xi} - \frac{n_i \mathbf{a}_i^0}{\sigma r_{1e}^0} \boldsymbol{\mu} \right), \quad (\text{A.23})$$

$$E(\rho) = \bar{F}(\rho),$$

^{||}To avoid further notation, we use the same symbol ϑ in (A.19) and in (A.10). However, $j(\boldsymbol{\eta}, \boldsymbol{\xi})$ in (A.19) represents a different and more general function than $j(\|\boldsymbol{\xi}\|)$ in (A.10).

**It can be shown that due to the symmetry of the summation ranges in (A.22) and (A.23), and the properties of the Dirac delta function, the choices of w and j satisfy (A.20).

for which (A.19) recovers (3.5), i.e., $\vartheta(\mathbf{x},t) = \rho_h(\mathbf{x},t)$, and $P(\mathbf{x},t) = -\bar{F}'(\rho_h(\mathbf{x},t))$ (cf. (A.12)). For the sake of the present comparison, we assume $\mathcal{B} = \mathbb{R}^3$. Under these choices, (A.21) recovers (3.4). This indeed demonstrates that the structureless MD EAM (3.1) in Section 3.1 can be upscaled to the generalized EAM-like PD model (A.21).

A.3.2 Structured MD EAM

We demonstrate that (4.11) is an EAM-like PD model. Specifically, we show that it represents an LPS model (cf. (A.6)). Let $j(\|\boldsymbol{\xi}\|) = 1/\|\boldsymbol{\xi}\|^{p-1}\chi^\varepsilon(\|\boldsymbol{\xi}\|)$ with

$$\chi^\varepsilon(\|\boldsymbol{\xi}\|) := \begin{cases} 1, & \|\boldsymbol{\xi}\| \leq \varepsilon, \\ 0, & \text{otherwise,} \end{cases}$$

a characteristic function. Then, by (4.12), (4.4), and (A.10),

$$\rho_h(\mathbf{x},t) = f_0\vartheta(\mathbf{x},t) \quad \text{and} \quad \frac{\rho_0}{f_0} \approx \vartheta_0.$$

We can now write (4.11) as

$$\begin{aligned} \rho(\mathbf{x}) \frac{\partial^2 \mathbf{u}}{\partial t^2}(\mathbf{x},t) = & \int_{\mathcal{H}(\mathbf{x},\varepsilon)} \left\{ \left[\frac{\bar{c}}{\vartheta_0} \left(\frac{\vartheta(\mathbf{x},t)}{\vartheta_0} - 1 \right) + \frac{\bar{c}}{\vartheta_0} \left(\frac{\vartheta(\hat{\mathbf{x}},t)}{\vartheta_0} - 1 \right) \right] j(\|\boldsymbol{\xi}\|) \right. \\ & \left. + \frac{\bar{k}}{\vartheta_0} \frac{1}{\|\boldsymbol{\xi}\|^p} (\|\boldsymbol{\xi} + \boldsymbol{\eta}\| - \|\boldsymbol{\xi}\|) \right\} \frac{\boldsymbol{\xi} + \boldsymbol{\eta}}{\|\boldsymbol{\xi} + \boldsymbol{\eta}\|} dV_{\hat{\mathbf{x}}} + \mathbf{b}(\mathbf{x},t) \end{aligned} \quad (\text{A.24})$$

with $\boldsymbol{\xi}$ and $\boldsymbol{\eta}$ defined in Section A.1.1. Equation (A.24) is an EAM-like PD model (cf. (A.11)) with

$$\begin{aligned} P(\mathbf{x},t) &= \frac{\bar{c}}{\vartheta_0} \left(1 - \frac{\vartheta(\mathbf{x},t)}{\vartheta_0} \right), \\ \kappa(\boldsymbol{\eta},\boldsymbol{\xi}) &= \chi^\varepsilon(\|\boldsymbol{\xi}\|) \frac{\bar{k}}{\vartheta_0} \frac{1}{\|\boldsymbol{\xi}\|^p} (\|\boldsymbol{\xi} + \boldsymbol{\eta}\| - \|\boldsymbol{\xi}\|). \end{aligned}$$

Let $\underline{\omega}\langle\boldsymbol{\xi}\rangle = j(\|\boldsymbol{\xi}\|)\|\boldsymbol{\xi}\|^{-1}$ be an influence function. Then, by (A.10) and (A.7), $\vartheta_0 = m$ is the weighted volume. Using relation (A.18), we can write (A.24) as

$$\rho(\mathbf{x}) \frac{\partial^2 \mathbf{u}}{\partial t^2}(\mathbf{x},t) = \int_{\mathcal{H}(\mathbf{x},\varepsilon)} \left\{ \frac{\bar{c}}{3m} [\theta[\mathbf{x},t] + \theta[\hat{\mathbf{x}},t]] \underline{\omega}\langle\boldsymbol{\xi}\rangle \underline{x}\langle\boldsymbol{\xi}\rangle + \frac{\bar{k}}{m} \underline{\omega}\langle\boldsymbol{\xi}\rangle \underline{e}[\mathbf{x},t]\langle\boldsymbol{\xi}\rangle \right\} \frac{\boldsymbol{\xi} + \boldsymbol{\eta}}{\|\boldsymbol{\xi} + \boldsymbol{\eta}\|} dV_{\hat{\mathbf{x}}} + \mathbf{b}(\mathbf{x},t),$$

with \underline{e} the extension scalar state (A.8) and \underline{x} the reference relative distance scalar state (cf. Section A.1.2). This represents an LPS model, i.e.,

$$\begin{aligned} \rho(\mathbf{x}) \frac{\partial^2 \mathbf{u}}{\partial t^2}(\mathbf{x},t) = & \int_{\mathcal{H}(\mathbf{x},\varepsilon)} \left\{ \left(\frac{3K-5G}{m} \right) [\theta[\mathbf{x},t] + \theta[\hat{\mathbf{x}},t]] \underline{\omega}\langle\boldsymbol{\xi}\rangle \underline{x}\langle\boldsymbol{\xi}\rangle + \frac{30G}{m} \underline{\omega}\langle\boldsymbol{\xi}\rangle \underline{e}[\mathbf{x},t]\langle\boldsymbol{\xi}\rangle \right\} \\ & \times \frac{\boldsymbol{\xi} + \boldsymbol{\eta}}{\|\boldsymbol{\xi} + \boldsymbol{\eta}\|} dV_{\hat{\mathbf{x}}} + \mathbf{b}(\mathbf{x},t), \end{aligned} \quad (\text{A.25})$$

with elastic moduli

$$G = \frac{\bar{k}}{30} \quad \text{and} \quad K = \frac{1}{9} \left(\bar{c} + \frac{1}{2} \bar{k} \right). \quad (\text{A.26})$$

Remark A.7. The two- and three-dimensional computations in Section 4.3 were performed with the LPS implementation in PDLAMMPS, using relations (A.26) to determine the corresponding elastic moduli in the LPS model.

References

- [1] F. Ercolessi, A molecular dynamics primer, available at <http://www.fisica.uniud.it/~ercolessi/md/> (1997).
- [2] M. S. Daw, M. I. Baskes, Semiempirical, quantum mechanical calculation of hydrogen embrittlement in metals, *Phys. Rev. Lett.* 50 (17) (1983) 1285–1288.
- [3] M. S. Daw, M. I. Baskes, Embedded-atom method: Derivation and application to impurities, surfaces, and other defects in metals, *Phys. Rev. B* 29 (12) (1984) 6443–6453.
- [4] F. H. Stillinger, T. A. Weber, Computer simulation of local order in condensed phases of silicon, *Phys. Rev. B* 31 (8) (1985) 5262–5271.
- [5] J. Tersoff, New empirical approach for the structure and energy of covalent systems, *Phys. Rev. B* 37 (12) (1988) 6991–7000.
- [6] M. Arndt, M. Griebel, Derivation of higher order gradient continuum models from atomistic models for crystalline solids, *Multiscale Model. Simul.* 4 (2005) 531–562.
- [7] P. Seleson, M. L. Parks, M. Gunzburger, R. B. Lehoucq, Peridynamics as an upscaling of molecular dynamics, *Multiscale Model. Simul.* 8 (1) (2009) 204–227.
- [8] S. A. Silling, Reformulation of elasticity theory for discontinuities and long-range forces, *J. Mech. Phys. Solids* 48 (2000) 175–209.
- [9] S. A. Silling, M. Epton, O. Weckner, J. Xu, E. Askari, Peridynamic states and constitutive modeling, *J. Elasticity* 88 (2007) 151–184.
- [10] R. B. Lehoucq, M. P. Sears, Statistical mechanical foundation of the peridynamic nonlocal continuum theory: Energy and momentum conservation laws, *Phys. Rev. E* 84 (2011) 031112.
- [11] W. A. Curtin, R. E. Miller, Atomistic/continuum coupling in computational materials science, *Modelling Simul. Mater. Sci. Eng.* 11 (2003) R33–R68.
- [12] W. K. Liu, E. G. Karpov, S. Zhang, H. S. Park, An introduction to computational nanomechanics and materials, *Comput. Methods Appl. Mech. Engrg.* 193 (2004) 1529–1578.
- [13] G. Lu, E. Kaxiras, Overview of multiscale simulations of materials, in: M. Rieth, W. Schommers (Eds.), *Handbook of Theoretical and Computational Nanotechnology*, Vol. X, American Scientific Publishers, 2005, Ch. 22, pp. 1–33.
- [14] M. J. Scott, E. Zaremba, Quasiatoms: An approach to atoms in nonuniform electronic systems, *Phys. Rev. B* 22 (4) (1980) 1564–1583.
- [15] J. K. Nørskov, Covalent effects in the effective-medium theory of chemical binding: Hydrogen heats of solution in the 3d metals, *Phys. Rev. B* 26 (6) (1982) 2875–2885.
- [16] F. Herman, S. Skillman, *Atomic Structure Calculations*, Englewood Cliffs, N.J.: Prentice-Hall, Inc., 1963.
- [17] S. M. Foiles, M. I. Baskes, M. S. Daw, Embedded-atom-method functions for the fcc metals Cu, Ag, Au, Ni, Pd, Pt, and their alloys, *Phys. Rev. B* 33 (12) (1986) 7983–7991.
- [18] R. A. Johnson, Analytic nearest-neighbor model for fcc metals, *Phys. Rev. B* 37 (8) (1988) 3924–3931.

- [19] J. H. Rose, J. R. Smith, F. Guinea, J. Ferrante, Universal features of the equation of state of metals, *Phys. Rev. B* 29 (6) (1984) 2963–2969.
- [20] D. J. Oh, R. A. Johnson, Simple embedded atom method model for fcc and hcp metals, *J. Mater. Res.* 3 (3) (1988) 471–478.
- [21] J. Mei, J. W. Davenport, G. W. Fernando, Analytic embedded-atom potentials for fcc metals: Application to liquid and solid copper, *Phys. Rev. B* 43 (6) (1991) 4653–4658.
- [22] B. V. Koten, M. Luskin, Analysis of energy-based blended quasi-continuum approximations, *SIAM J. Numer. Anal.* 49 (2011) 2182–2209.
- [23] S. J. Plimpton, Fast parallel algorithms for short-range molecular dynamics, *J. Comp. Phys.* 117 (1995) 1–19, available at <http://lammps.sandia.gov>.
- [24] M. L. Parks, R. B. Lehoucq, S. J. Plimpton, S. A. Silling, Implementing peridynamics within a molecular dynamics code, *Comp. Phys. Comm.* 179 (11) (2008) 777–783.
- [25] M. L. Parks, P. Seleson, S. J. Plimpton, R. B. Lehoucq, S. A. Silling, Peridynamics with LAMMPS: A user guide, Tech. Rep. SAND2010-5549, Sandia National Laboratories (2010).
- [26] E. Askari, F. Bobaru, R. B. Lehoucq, M. L. Parks, S. A. Silling, O. Weckner, Peridynamics for multiscale materials modeling, in: *SciDAC 2008*, 13-17 July, Washington, Vol. 125 of *J. Phys.: Conf. Ser.*, IOP Publishing, 2008, p. 012078.
- [27] B. Alali, R. Lipton, Multiscale dynamics of heterogeneous media in the peridynamic formulation, *J. Elasticity* 106 (1) (2012) 71–103.
- [28] B. Kilic, E. Madenci, Coupling of peridynamic theory and the finite element method, *J. Mech. Mater. Structure* 5 (5) (2010) 707–733.
- [29] R. W. Macek, S. A. Silling, Peridynamics via finite element analysis, *Finite Elem. Anal. Des.* 43 (2007) 1169–1178.
- [30] P. Seleson, S. Beneddine, S. Prudhomme, A force-based coupling scheme for peridynamics and classical elasticity, *Comput. Mater. Sci.* 66 (2013) 34–49.
- [31] G. Lubineau, Y. Azdoud, F. Han, C. Rey, A. Askari, A morphing strategy to couple non-local to local continuum mechanics, *J. Mech. Phys. Solids* 60 (2012) 1088–1102.
- [32] F. Han, G. Lubineau, Coupling of nonlocal and local continuum models by the Arlequin approach, *Int. J. Numer. Meth. Engr.* 89 (2012) 671–685.
- [33] S. A. Silling, E. Askari, A meshfree method based on the peridynamic model of solid mechanics, *Comp. Struct.* 83 (2005) 1526–1535.
- [34] A. C. Eringen, *Nonlocal Continuum Field Theories*, Springer, New York, 2002.
- [35] E. Kröner, Elasticity theory of materials with long range cohesive forces, *Int. J. Solids Structures* 3 (5) (1967) 731–742.
- [36] I. A. Kunin, *Elastic Media with Microstructure I: One-dimensional Models*, Vol. 26 of *Springer Series in Solid State Sciences*, Springer-Verlag, Berlin, 1982.
- [37] I. A. Kunin, *Elastic Media with Microstructure II: Three-dimensional Models*, Vol. 44 of *Springer Series in Solid State Sciences*, Springer-Verlag, Berlin, 1983.
- [38] D. Rogula, Introduction to nonlocal theory of material media, in: D. Rogula (Ed.), *Nonlocal Theory of Material Media*, Springer-Verlag, Berlin, 1982, pp. 125–222.
- [39] W. Noll, Die herleitung der grundgleichungen der thermomechanik der kontinua aus der statistischen mechanik, *J. Ration. Mech. Anal.* 4 (1955) 627–646.
- [40] S. A. Silling, R. B. Lehoucq, Convergence of peridynamics to classical elasticity theory, *J. Elasticity* 93 (2008) 13–37.
- [41] P. Seleson, M. L. Parks, On the role of the influence function in the peridynamic theory, *Int. J. Multiscale Comput. Engr.* 9 (6) (2011) 689–706.